Materials Today Chemistry 30 (2023) 101489

Contents lists available at ScienceDirect

Materials Today Chemistry

journal homepage: www.journals.elsevier.com/materials-today-chemistry/

Theoretical approach to the one-step versus two-step spin transitions in Hofmann-like Fe^{II} SCO metal-organic frameworks

D. Arias-Olivares, R. Sánchez-de-Armas, C.J. Calzado*

Departamento de Química Física, Universidad de Sevilla, C/ Prof. García González, s/n, 41012 Sevilla, Spain

ARTICLE INFO

Article history:
Received 25 November 2022
Received in revised form
26 January 2023
Accepted 3 March 2023
Available online xxx

Keywords:
Hofmann Fe(II) spin-crossover metal-organic frameworks
DFT calculations
Ab-initio ligand field parameters
CASSCF/NEVPT2 calculations
Guest-guest interactions
Host-guest interactions

ABSTRACT

Guest molecules in the 3D Hofmann-type Fe^{II} spin-crossover (SCO) metal-organic frameworks modulate the magnetic properties of the host, modifying the spin state, transition temperature, width of the hysteresis loop and are responsible for the occurrence of a single-step or multistep spin transition. In this work we explore the guest-dependent SCO properties of the Hofmann-like Fe^{II} SCO clathrates with formula $\{Fe(bpb)[Pt(CN)_4]\}\cdot 2G$. We use a computational strategy based on DFT periodic calculations on the whole system, CASSCF/NEVPT2 calculations on single metal fragments and plots of the reduced density gradients to identify and quantify the dominant effects governing the occurrence of one-step or two-step spin transitions in these systems. Our results inform about the strength of the ligand field around Fe sites, the relative stability of the different spin states, the amplitude and nature of the host-guest and guest-guest interactions, and the role of the vibronic effects on the SCO properties of Hofmann-type Fe^{II} clathrates.

© 2023 The Author(s). Published by Elsevier Ltd. This is an open access article under the CC BY-NC-ND license (http://creativecommons.org/licenses/by-nc-nd/4.0/).

1. Introduction

Since Kitazawa and co-workers synthesized the first Hofmann-type coordination polymer displaying spin-crossover (SCO) behavior [1], the SCO Hofmann-type family has received widespread attention and rapidly grown following different synthetic strategies [2–6]. Hofmann-like Fe^{II} SCO clathrates are the most popular [5,7], combining the chemical stability, porosity and tunability of 2D and 3D metal-organic frameworks (MOFs) with the Fe^{II} SCO phenomenon. This property refers to the transition between the high spin ($S = 2$; $t_{2g}^4 e_g^2$) and the low spin ($S = 0$; $t_{2g}^6 e_g^0$) states of the Fe centers. The switch can be triggered by an external stimulus such as light, temperature, pressure, among others, that produces magnetic, structural, or optical changes as a response [8–20].

In the case of Hofmann SCO clathrates, the SCO properties can be modulated by the presence of guest molecules within the pores of the host framework [6,21–26]. Hofmann 3D Fe^{II} SCO clathrates have the general formula $\{Fe(L)[M^{II}(CN)_4]\}\cdot G$ and $\{Fe(L)[M^{I}(CN)_2]_2\}\cdot G$ with L being a pillaring bis-monodentate pyridine-like ligand, M^{II} = Ni, Pd, Pt, M^{I} = Cu, Ag, Au and G being the guest molecule [21,27]. If monodentate ligands are used (usually pyridine derivatives), a 2D network is obtained with a general formula of $\{Fe(L)_2[M^{II}(CN)_4]\}$. Their structure is based on planar layers, where quasi-octahedral Fe^{II} ions alternate with divalent group 10 metal centers, bonded to four cyanide ligands in a square planar geometry. The layers are interconnected by nitrogen-containing ligands, where nitrogen atoms occupy the axial position of Fe centers (Fig. 1).

The 3D Fe^{II} SCO-MOFs have permanent porosity and, depending on the nature and load of guest per Fe site different SCO behaviors have been reported [2,28–31], ranging from abrupt single step to multistep spin transitions, with transition temperatures that can be shifted to room temperature, providing the system with sensing properties toward guest adsorption.

The guest dependent SCO behavior is related to electronic and steric effects [23,32,33] such as the size and shape of the guest molecules, the pore loading content, the location and arrangement of the guest, the chemical properties of the guest, the cavity of the host, the interaction type and strength (π-stacking, C–H$\cdots\pi$ and guest … M' contacts, hydrogen bonding interactions), … The subtle balance between the competition and cooperation of these effects makes it difficult to establish clear and universal relationships between SCO and the host-guest interactions. In fact, some experiments have recently shown that even slight changes in these

* Corresponding author.
E-mail address: calzado@us.es (C.J. Calzado).

https://doi.org/10.1016/j.mtchem.2023.101489
2468-5194/© 2023 The Author(s). Published by Elsevier Ltd. This is an open access article under the CC BY-NC-ND license (http://creativecommons.org/licenses/by-nc-nd/4.0/).

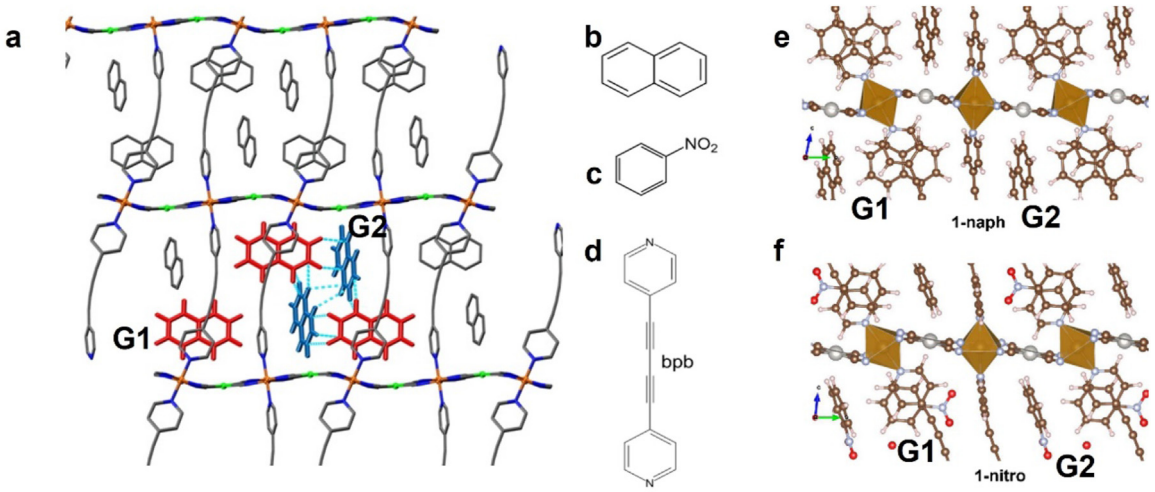

Fig. 1. (a) General representation of the MOF. The two different crystallographic positions for the guest molecules are highlighted in red (G1) and blue (G2). The horizontal layers contain the Fe octahedrons and the metal-cyanides units. These layers are connected through pillaring ligands as bpb (d). Naphthalene (b) and nitrobenzene (c) are the guest molecules considered in this work. (e, f) Relative orientation of the Fe octahedrons with respect to the layers containing the metal-cyanides units for both systems. The octahedrons close to G1 molecules are more tilted in 1-nitro than 1-naph.

interactions can lead to completely different SCO behaviors [26,31,34].

It is the aim of this work to reveal and quantify the different physical effects giving rise to the two-step transition in Hofmann-like Fe^{II} SCO clathrates. We have investigated by means of quantum chemistry-based calculations the synergic effects of the geometrical conformation, the vibrational contribution to the lattice dynamic, the host–guest and guest-guest interactions, and the ligand field strength of Fe^{II} centers. We focus in two Hofmann-like Fe^{II} SCO clathrates with formula $\{Fe(bpb)[Pt(CN)_4]\}\cdot 2G$, synthesized and characterized by Real and co-workers [35] (Fig. 1), with *bpb* = bis(4-pyridyl)butadiyne acting as the pillaring ligand. The system presents a two-step transition when the guest molecule is naphthalene (**1-naph**), while for nitrobenzene (**1-nitro**) the spin switching occurs in a single step. Similar behavior has been found for parent compounds containing Ag, Ni, Pd, and Zn [2,28].

Our results indicate that the ligand field experienced by Fe sites is not the leading effect governing the dissimilar SCO properties of these two systems, but intramolecular and intermolecular interactions. Our main contribution consists in the evaluation of these host-guest and most importantly guest-guest interactions, which consistently reflect their nature and strength, and can be considered at the origin of the differential SCO behavior of these two Fe^{II} Hofmann clathrates.

2. Description of the system and computational details

Systems **1-naph** and **1-nitro** were synthesized and characterized by Real et al. [35]. They are isostructural, both crystalized in the triclinic $P\bar{1}$ space group. The special bent conformation of the *bpb* ligand allows the pyridine moieties to locate slightly perpendicular to each other and provides the largest available guest free volume of the isoreticular series $\{Fe(L)[M(CN)_4]\}\cdot G$ [2]. Hence the accessible volume at low temperature is 849.6 $Å^3$ and 801.8 $Å^3$ for **1-naph** and **1-nitro,** corresponding to 53.8% and 52.6% of the unit cell volume, respectively. In system **1-naph**, the spin transition occurs in two steps with critical temperatures of $T_{c1}^{\downarrow} = 205$ K and $T_{c2}^{\downarrow} = 188$ K in the cooling mode and $T_{c2}^{\uparrow} = 203$ K and $T_{c1}^{\uparrow} = 216$ K in the heating way. This results in two hysteresis loops of 11 K and 15 K wide. The average changes of the enthalpy and entropy for the high- and low-temperature loops are: $\Delta H_1 = 9.45$ kJ/mol, $\Delta S_1 = 44.9$ JK/mol and $\Delta H_2 = 8.62$ kJ/mol, $\Delta S_2 = 44.1$ JK/mol, respectively. On the contrary in system **1-nitro**, the spin transition takes place in one step at $T_c^{\downarrow} = 210$ K and $T_c^{\uparrow} = 237$ K, with a hysteresis loop of 27 K wide and $\Delta H = 19.29$ kJ/mol and $\Delta S = 86.3$ JK/mol.

There are two crystallographic different positions in the voids of the MOF that can be occupied by the guest molecules, G1 and G2 (Fig. 1). Molecules in position 1 are sandwiched between the pyridyl group of the *bpb* ligands connected to two neighbor Fe_1 centers, while molecules in position 2 are in between Fe_1 and Fe_2 octahedrons, parallel to the pyridyl group connected to Fe_2 center, but rotated about 90° with respect to the pyridyl of Fe_1 site, in a T-shaped configuration.

2.1. Optimization and evaluation of the thermodynamic data

The computational models were built on the basis of the available crystallographic data of the synthesized compounds (CCDC 971021–971,025) [35]. For both systems, the unit cell contains two Fe^{II} centers and four guest molecules. To study the spin crossover behavior, three possible spin configurations were modeled: high spin or low spin for both Fe centers (HSHS and LSLS solutions) and a mixed spin solution (HSLS). For system **1-naph,** the available X-ray data corresponds to structures at 120, 195 and 250 K, matching the LSLS, mixed HSLS and HSHS states, while for system **1-nitro,** we built a model for the hypothetic mixed-spin HSLS solution starting from the available high (250 K) and low (120 K) temperature crystallographic data. Two independent optimizations were carried out, resulting two quasi-degenerate models. The results reported hereafter concerns the most stable one, obtained from the low temperature X-ray data, with Fe_1 and Fe_2 centers in high and low spin configuration, respectively.

The whole system (MOF and guest) was optimized employing periodic boundary conditions in the frame of the density functional theory (DFT). The optimizations, carried out with the Vienna *ab-initio* simulation package (VASP) [36–39], include the lattice parameters of the unit cell and the atomic positions. The revised Perdew–Burke–Ernzerhof (rPBE) [40] functional was used as in previous studies dealing with SCO compounds [41–44]. The van der Waals dispersion effects were included by the DFT-D3 method of Grimme et al. with Becke-Johnson damping [45,46]. The projector-

augmented wave (PAW) [47] potentials were employed for all the atoms. All the calculations refer to the Γ-point of Brillouin's zone, with an energy cut-off of 800 eV for the plane-wave basis set representing the valence electrons. Electronic relaxation was performed until the change in the total energy between two consecutive steps is smaller than 10^{-6} eV and the ionic relaxation has been performed until the Hellmann−Feynman forces were lower than 0.01 eV/Å.

To obtain the different solutions the spin-polarized calculations were constrained to a fixed difference between the number of electrons in the spin up (N_α) and spin down (N_β) components (NUPDOWN option in VASP code). Hence, the HSHS, HSLS and LSLS configurations require an N_α-N_β = 8 (four unpaired electrons at each Fe center), N_α-N_β = 4, and $N_\alpha = N_\beta$, respectively.

To compare with the experimental data, the transition enthalpy and entropy were also evaluated. As well known, the enthalpy variation associated to the SCO can be separated in different contributions: $\Delta H(T) = \Delta E_{elec} + \Delta ZPE + \Delta H_{vib} + \Delta H_{rot} + \Delta H_{trans}$, where ΔE_{elec} corresponds to the difference of the computed energy for the HS and LS solutions, ΔZPE is the difference between the zero-point vibrational energy, and ΔH_{vib}, ΔH_{rot} and ΔH_{trans} are the vibrational, rotational and translational thermal contributions to the transition enthalpy. Similarly, the transition entropy can be separated as $\Delta S(T) = \Delta S_{elec} + \Delta S_{vib} + \Delta S_{rot} + \Delta S_{trans}$.

In the harmonic approximation, the ΔZPE can be evaluated as one-half of the sum of the vibrational frequency shifts upon the spin transition:

$$\Delta ZPE = \frac{1}{2} h \sum_i [\nu_i(HS) - \nu_i(LS)]$$

The translational and rotational contributions to the transition enthalpy and entropy can be neglected and consider only the dominant vibrational and electronic parts. The vibrational contribution to the total enthalpy and entropy are computed as follows [9,48]:

$$H_{vib}(T) = \sum_i \frac{h\nu_i e^{-\frac{h\nu_i}{k_B T}}}{1 - e^{-\frac{h\nu_i}{k_B T}}} \quad S_{vib}(T)$$
$$= R \sum_i \left[-\ln\left(1 - e^{-\frac{h\nu_i}{k_B T}}\right) + \frac{h\nu_i}{k_B T} \frac{1}{e^{\frac{h\nu_i}{k_B T}} - 1} \right]$$

The electronic contribution to the entropy can be considered as a good approximation to be temperature independent and computed as $S_{elec} = Rln(2S + 1)$, with S equals to the total spin of the system. Hence, it is mandatory the computation of the normal vibration modes to get the vibrational contribution to the thermodynamic expressions. The second-order derivatives of the total energy have been evaluated using the finite differences approach, with exigent criteria in the optimization runs to obtain the complete set of real frequencies (all forces were lower than 0.01 eV/Å with an accurate precision mode, PREC=Accurate).

Although it is usual to consider ΔS_{vib} and ΔH_{vib} almost independent on the temperature during the spin transition, it has been previously noted by Robert et al. [49] that this approximation could be questionable in the case of Fe SCO complexes. Fig. S3 represents ΔS and ΔH for systems **1-naph** and **1-nitro** at temperatures ranging from 120 K to 250 K, the transition enthalpy shows a slight dependence with temperature (about 6%) while the entropy is much more sensitive (changes of 30% in the considered temperature range). Hence, we report in Table 2 the enthalpy and entropy values obtained at the mean transition temperature ($T_c\uparrow + T_c\downarrow$)/2 for each step, i.e., 196.5 K and 209.5 K for system **1-naph** and 223.5 K for system **1-nitro**.

2.2. Ab initio ligand field parameters

We have also evaluated the ligand field around Fe sites using the *ab-initio ligand field theory* (AILFT) [50] approach implemented in ORCA 5.0.3 package [51]. Each Fe center was modeled separately, using the optimized geometry obtained from the periodic DFT calculations on the whole crystal. The model contains the close 4 CN ligands and the pyridyl groups of the *bpb* ligand in the axial positions. The rest of the *bpb* ligand was removed and replaced by an extra hydrogen atom, with C−H bond length of 1.085 Å, the mean value of the pyridyl C−H bond lengths.

State-average complete-active space self-consistent field (CASSCF) calculations were done with active spaces containing 6 electrons of Fe^{II} center in the 3d orbitals, i.e. CAS(6,5). All the roots with spin multiplicity of 5, 3 and 1 (5, 45, and 50 roots, respectively) were considered. The total energy was corrected with the inclusion of dynamical correlation effects through the strongly contracted version of the NEVPT2 approximation [52−55]. Basis sets of quality SVP [56] were used for all atoms, except for Fe modeled with the def2-TZVPP basis set [57,58].

2.3. Non-covalent interactions

The non-covalent interactions between the guest molecules and the MOF were analyzed via NCIPlot4 code [59], using the clustering approximation to provide insights in the MOF-guest interaction [60]. This approach uses the electron density and its derivative to visualize the non-covalent interactions as real-space surfaces. The central idea is that the regions far from the molecule in which the density ρ decays to zero exponentially, the reduced gradient s, ($s = 1/(2(3\pi^2)^{1/3})|\nabla\rho|/\rho^{4/3}$) will have very large positive values, while for regions of both covalent bonding and non-covalent interactions, the reduce gradient takes very small values. To distinguish between these interactions, the sign and amplitude of the

Table 1
Selected bond lengths (Å) and cell volume (Å^3) for 1-**naph** and **1-nitro** in the optimized HSHS, HSLS and LSLS electronic configurations. Available experimental data in parentheses. RMSD refers to the root-mean-square displacements of the optimized atomic positions with respect to the experimental ones (Å).

	1-naph			1-nitro		
	HSHS	HSLS	LSLS	HSHS	"HSLS"	LSLS
Volume	1637.44	1582.22	1543.33	1528.37	1535.10	1493.33
Fe_2−$N_{11,12}$	2.11 (2.116)	1.89 (1.938)	1.89 (1.938)	2.09 (2.161)	1.89	1.89 (1.937)
Fe_2−$N_{3,4}$	2.08 (2.106)	1.88 (1.935)	1.88 (1.935)	2.08 (2.145)	1.89	1.89 (1.933)
Fe_2−$N_{1,2}$	2.14 (2.193)	1.96 (2.000)	1.96 (1.996)	2.16 (2.232)	1.96	1.97 (1.997)
Fe_1−$N_{7,8}$	2.10 (2.127)	2.10 (2.127)	1.90 (1.944)	2.11 (2.168)	2.08	1.89 (1.934)
Fe_1−$N_{5,6}$	2.06 (2.115)	2.07 (2.124)	1.88 (1.935)	2.08 (2.141)	2.09	1.88 (1.933)
Fe_1−$N_{9,10}$	2.17 (2.189)	2.17 (2.229)	1.97 (2.001)	2.15 (2.199)	2.16	1.96 (2.000)
RMSD	0.43	0.32	0.25	0.61	No data	0.22

Table 2
Relative energy ΔE_{elec} for the optimized structures, zero-point correction ΔZPE, transition enthalpy ΔH and entropy ΔS per Fe center evaluated at the experimental mean critical temperature $(T_c\uparrow + T_c\downarrow)/2$. Energy values in kJ/mol, transition entropy in J/mol/K.

	1-naph		1-nitro
	HSHS-HSLS	HSLS-LSLS	HSHS-LSLS
ΔE_{elec}	39.8	33.5	70.7
ΔZPE	−8.1	−6.8	−14.1
ΔH	34.9	29.2	62.0
ΔS	45.1	40.0	54.9

second eigenvalue of the electron-density Hessian matrix, λ_2, is employed [61]. Hence, it is possible to distinguish bonded $\lambda_2 < 0$ to non-bonded contacts $\lambda_2 > 0$, while very weak, van de Waals interactions present very low densities ($\rho \approx 0$) and very low Hessian eigenvalues $\lambda_2 \approx 0$. Here, only values close to zero were found, indicating weak and attractive non-covalent interactions. The gradient isosurfaces (s = 0.03 au) are represented in Fig. 6. The π-π stacking is depicted as a green plateau, while the other attractive non-covalent interactions correspond to small green rods.

A 2 × 2 × 2 supercell was constructed for system **1-naph** and 3 × 3 × 3 supercell for system **1-nitro** to ensure a representative environment for the inner guest. The code plots only the interactions around the guest molecule within a radius of 2.0 Å (keyword LIGAND of NCIPlot4) [62]. The electron density was obtained by means of the *promolecular* approximation (independent atom model) which is in qualitative agreement with the density provided by self-consistent methods [63]. It is worth to mention that recently the NCI approach in combination with the *extremely localized molecular orbitals* (ELMO-NCI methodology) have been presented as potential tool to be applied to MOFs with periodic DFT approaches [64].

3. Results

3.1. Geometries and transition parameters

Both systems were fully optimized for each electronic configuration and the frequencies of the normal vibration modes computed, ensuring that the calculated geometries are minima on the potential energy surface. Selected geometric parameters are collected in Table 1 and optimized cell parameters reported in Table S1. Fig. 2 shows a detail of the cyanide-bridged Fe^{II}—Pt^{II} bimetallic 3D network. The root-mean square displacement (RMSD) of the optimized structure for each electron configuration with respect to the crystallographic data was evaluated with the VMD code [65], aligning as pivot the Fe and Pt atoms, while the whole cell is computed. The RMSD values indicate a nice agreement with the experimental data, in particular for the LS solution in both systems.

In the transition from HS to LS, the Fe centers increase their local symmetry from D_{2h} to D_{4h} in both systems, but the guest just introduces rather small differences in the average Fe—N bond distances. However, the distortion of the Fe octahedrons with respect to the plane of the $Pt(CN)_4$ units is larger for **1-nitro** than **1-naph** (Fig. 2).

The LSLS configuration presents a significant volume contraction with respect to HSHS solution, as usual for this type of compounds, the change of volume corresponds to 94.0 $Å^3$ (5.7%) and 35.0 (2.2%) $Å^3$ in **1-naph** and **1-nitro**, respectively. Fig. 3 shows the superposition of the HSHS and LSLS geometries for each system, the contraction of the MOF when going from the HSHS configuration to the LSLS is notorious around the metal and pyridyl groups.

Among the effects usually invoked to explain the guest-dependent SCO properties of Hofmann clathrates, the ligand field around Fe site and the way it is modified by the guest occupy a predominant place. It has been suggested that the weaker the ligand field around Fe site, the higher the probability of a two-step spin transition [66–68]. The ligand field strength of the Fe site on each spin state was evaluated by means of the *ab-initio* ligand field theory. Fig. 4 recreates the transition steps for Fe_1Fe_2 from HS_1HS_2 (left) $\rightarrow HS_1LS_2$ (middle) $\rightarrow LS_1LS_2$ (right). The separation between the barycenters of the t_{2g}- and e_g-like orbitals, Δ_0, is about 10,000 cm^{-1} for the HS phase and 20,000 cm^{-1} for the LS states, in line with previous evaluations for molecular Fe^{II} SCO complexes [41,42]. The ligand field parameters are sensitive to the local environment of each site, showing Δ_0 values slightly different for Fe_1 and Fe_2 centers in the same spin state, in line with the observed (small) geometrical differences (Table 1). In general, the field is slightly stronger for Fe center close to the guest molecule in position 2 (center Fe_2). The largest difference is observed for the HS state of system **1-nitro**, where the Δ_0 values of Fe_1 and Fe_2 differ by about 400 cm^{-1}. For this state, the ligand field is the weakest of all considered. However, non-significant differences are found between **1-nitro** and **1-naph** that can justify the dissimilar SCO behavior. It is interesting to note that in the intermediate state, the spin transition in the first center does not induce substantial changes in the field of the neighboring center, what was suggested as a likely effect in the case of dinuclear Fe^{II} SCO with two-step transitions [67].

Regarding the relative stability, the LSLS configuration is the most stable in line with the experimental data, the separation with the HSHS state is about 70 kJ/mol (ΔE_{elec} = 73.3 and 70.7 kJ/mol for **1-naph** and **1-nitro**, respectively). As stated previously [66–69], the relative stabilization of the intermediate state HSLS with respect to the barycenter of the HSHS-LSLS gap is a necessary condition for the occurrence of a two-step transition. For system **1-naph**, we found that the HSLS lies 3.1 kJ/mol below the barycenter (−δ), in line with the observed two-step transition (Fig. 5), while in the case of system **1-nitro,** our model for the hypothetic HSLS state lies 1.6 kJ/mol above the barycenter (+δ), in accordance with a single step transition. It is also relevant that the cell volume of this hypothetic intermediate state does not follow the expected trend (Table 1), the calculated volume being larger than that obtained for the pure HS state.

Thermodynamical analysis had been developed according with the equations exposed previously (Table 2). The computed transition enthalpy values for **1-naph** are ΔH_1 = 29.2 and ΔH_2 = 34.9 kJ/mol for the two successive transitions in the heating mode. In the

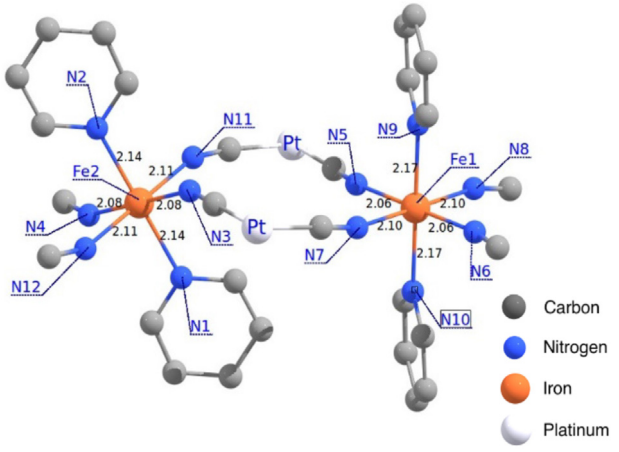

Fig. 2. Structural analysis for **1-naph** and **1-nitro**. For clarity, the hydrogen atoms were omitted and only the first neighbor atoms around Fe centers are shown. Bond distances (Å) for **1-naph** system in the HSHS state are included, the complete data set is reported in Table 1.

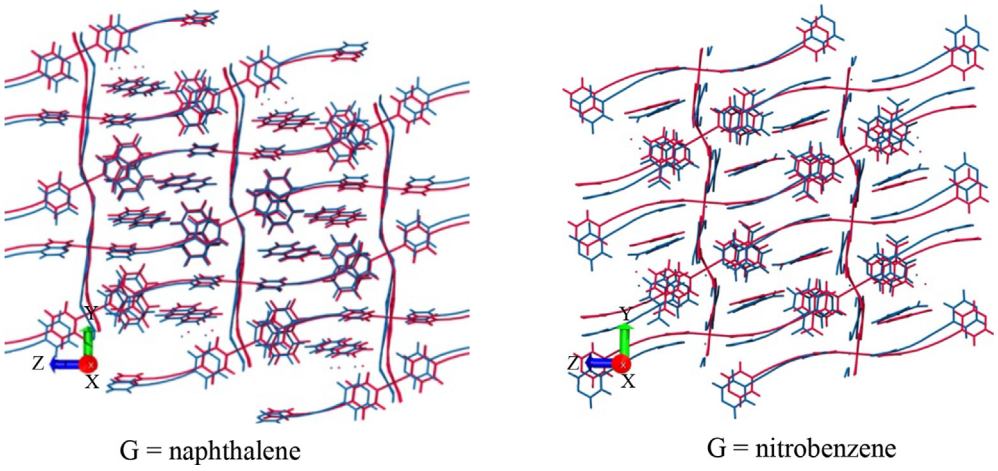

Fig. 3. Superposition of HSHS (blue) and LSLS (red) configurations for systems **1-naph** and **1-nitro**.

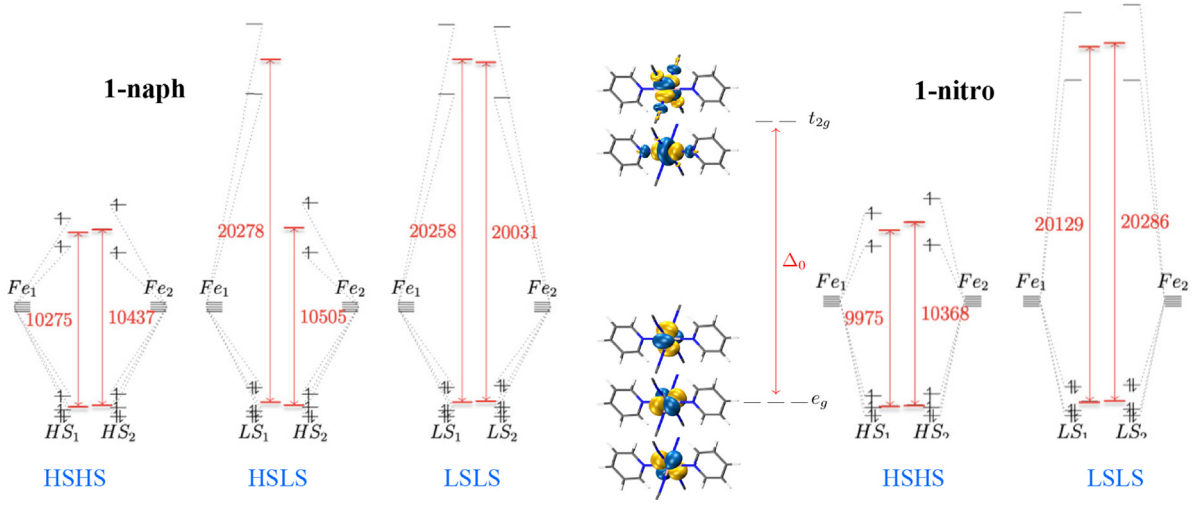

Fig. 4. Ab-initio ligand field parameters for Fe centers in systems **1-naph** and **1-nitro**. The ligand field strength Δ_0 (in cm^{-1}) is measured between the barycenters (in red) of the t_{2g}-like and e_g-like orbitals.

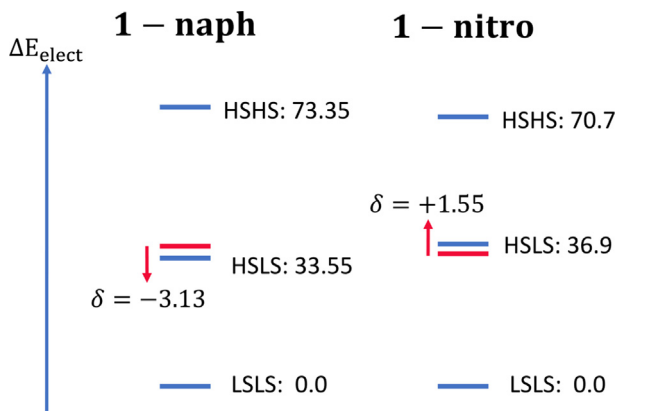

Fig. 5. Relative electronic energy for each state in kJ/mol. The red line represents the barycenter and the mixed state shows the $\pm\delta$ displacement around the barycenter.

case of **1-nitro**, the computed transition enthalpy between the pure HS and LS states is of 62.0 kJ/mol. These values are overestimated with respect to the experimental ones as usual for the DFT-based evaluations of the Fe SCO complexes [24,69–73]. Better agreement can be found by using TPSSh functional [69,73] or DFT + U approach [74]. Unfortunately, the former is quite expensive for a periodic scheme, while DFT + U presents the bias of the choice of the on-site Coulomb interaction U. Notice that despite the overestimation, the computed values correctly predict the ratio between ΔH_1 and ΔH_2 in system **1-naph** ($\Delta H_2/\Delta H_1$ ~1.1), as well as the ratio with the transition enthalpy of **1-nitro**. The calculated transition entropy is nicely in good agreement with the experimental data for both systems (44.1 and 44.9 Jmol/K for **1-naph**, and 86.3 Jmol/K for system **1-nitro**).

3.2. Intermolecular host-guest and guest-guest interactions

The unit cell of the MOF contains two Fe sites and four guest molecules. Different host-guest and guest-guest interactions can be envisaged and isolated by specific single-point calculations. The average interaction energy of the guest molecules with the host is calculated as follows:

$$E_{int}(\text{host}-\text{guest}) = \left[E_{sys} - (E_H + 4E_G)\right] / 4$$

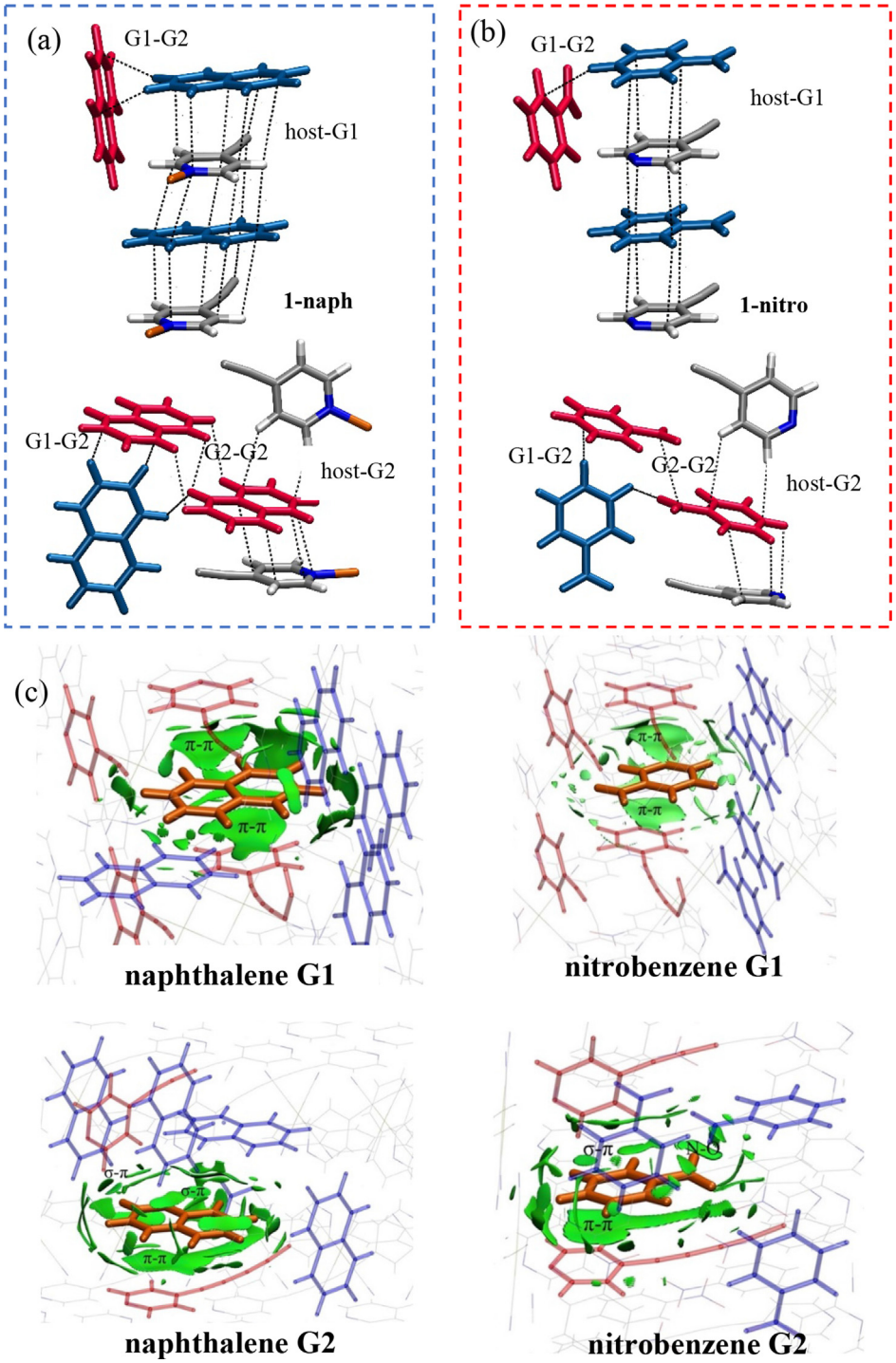

Fig. 6. Short contacts between host and guest molecules in position 1 (blue molecule) and position 2 (red molecule) for (a) naphthalene and (b) nitrobenzene guest molecules. Note that G1-G1 interaction is hindered by the presence of the pyridyl rings of the bpb ligand. (c) Gradient isosurfaces (s = 0.03 au) representing non-covalent interactions for encapsulated naphthalene and nitrobenzene (in brown) in positions 1 and 2 based on the HS geometries. Green regions represent weak interactions with the MOFs (red fragments) and close guest molecules (blue fragments).

where E_{sys} corresponds to the total energy of the MOF with four guest molecules occupying the voids of the unit cell, E_H is the energy of the MOF in absence of guests, but with the same geometry than the whole system, and E_G is the energy of an isolated guest molecule.

As mentioned, there are two different positions in the voids of the MOF that can be occupied by the guest molecules, G1 and G2. To distinguish between them, we have calculated the interaction energy of the host with molecules G1 and G2 separately as follows:

$$E_{int}(host - G1) = [E_{HG1} - (E_H + 2E_G)] / 2$$

$$E_{int}(host - G2) = [E_{HG2} - (E_H + 2E_G)] / 2$$

where E_{HG1} (E_{HG2}) is the total energy of the MOF containing just guest molecules in position 1 (position 2), calculated with the optimized geometry of the whole system.

Guest molecules occupying position 1 in the void cannot interact among themselves, since they are sandwiched between the pyridyl rings of the *bpb* ligands (Fig. 6a), but they can interact with the neighbor guest molecules in position 2. It is possible to evaluate the amplitude of this interaction as $E_{int}(G1-G2) = [E_{G1G2} - (E_{G1} + E_{G2})]/2$. E_{G1G2} is obtained from single point calculation of the four guest molecules in the geometry resulting from the optimization of the whole system. E_{G1} and E_{G2} refer instead to single-point calculations with two guest molecules on position 1 or 2, respectively. Also, there exists the possibility of intermolecular interactions between molecules in position 2, with energy $E_{int}(G2-G2) = E_{G2} - (2E_G)$.

Table 3 collects the different interaction energies for **1-naph** and **1-nitro** on the high and low-spin states. These values can be compared with the adsorption enthalpy of N_2 and CO_2 on the parent [Fe(pz)Ni(CN)$_4$] Hofmann clathrate [75] with values of 15–20 kJ/mol and 30 kJ/mol, respectively, estimated from the gas adsorption isotherms. In general, the interactions between the guest molecules and the MOF are stronger for naphthalene than nitrobenzene, the adsorption energies being slightly spin-dependent, larger for the LS configuration than the HS one. This is in line with the fact that the number of host-guest and guest-guest intermolecular contacts decreases in the HS state [2], due to the change of volume associated with the population of this state.

This result contrasts with the behavior observed by Aravena et al. [24] in related [Fe(pz)Pt(CN)$_4$] compound, with higher interaction energies for the high-spin state. It is important to note that the MOF family explored by Aravena corresponds to frameworks with smaller available volume, where the size effect of the guest molecules play a major role. Here, however, the pillaring *bpb* ligand maximizes the available volume of the unit cell, and the size of the guest should not be the effect controlling the occurrence of a one- or two-step spin transition, but the number and strength of the intermolecular interactions.

The preferred adsorption site is position 1 both for naphthalene and nitrobenzene, with very close interactions energies (Table 3). In this position, the guest molecule is sandwiched between two pyridyl rings of the *bpb* ligands, stabilized by face-to-face π-π interactions (similar short π-π contacts for both systems: 3.705 Å, 3.503 Å **1-nitro** HSHS, 3.548 Å, 3.649 Å **1-nitro** LSLS; 3.644 Å, 3.711 Å **1-naph** HSHS, 3.588 Å, 3.787 Å **1-naph** LSLS) (Fig. 6). The slightly shortest contacts for **1-nitro** LSLS can account for the strongest host-G1 interactions. Guest molecules in position 2 present weaker interactions with the MOF, in particular for nitrobenzene. In this position 2, the guest molecule interacts with the pyridyl groups of two close *bpb* ligands (Fig. 6). One interaction is driven by the face-to-face π packing between the rings, at larger distances than in position 1 (3.895 Å, 3.950 Å **1-nitro** HSHS, 3.848 Å, 3.901 Å **1-nitro** LSLS; 3.678 Å, 3.671 Å, **1-naph** HSHS, 3.686 Å, 3.511 Å **1-naph** LSLS) and with larger relative slippage of the π rings in the case of **1-naph**, while the second interaction is controlled by edge-to-face σ-π type interactions between the C–H bonds and π orbitals of the rings (Fig. 6). These host-G2 interactions are greater for **1-naph** than **1-nitro** and can act as an internal pressure effect disfavoring the HS to LS conversion and assisting the two-step transition.

Additional guest-guest intermolecular interactions can be distinguished: G2-G2 interactions between guest molecules in position 2 (Fig. 6) and G1-G2 interactions between molecules in position 1 and 2. The strength of these interactions is noticeable representing a significant percentage of the host-guest ones (about 30–40%). Considering that each molecule is involved in several of these interactions (Fig. S5), they can be responsible for the different SCO behavior of **1-naph** and **1-nitro**.

The intermolecular G2-G2 interactions are offset π-π in nature, while G1-G2 interactions are of edge-to-face σ(C–H). π type (Fig. 6). These two intermolecular interactions are stronger for **1-naph** than **1-nitro**, as puts in evidence the green surfaces in Fig. 6c, smaller in the case of nitrobenzene. This can be attributed to the presence of the nitro group, an electron withdrawing group that decreases the π electronic density in the benzene ring and attenuate the edge-to-face and offset π interactions. In the case of **1-nitro** the G2-G2 interaction is particularly weak for the LSLS state (Table 3). In fact, the analysis of the non-covalent interactions suggests the presence of repulsive $NO_2\cdots NO_2$ interactions in the LS form, absent in the HS state (Fig. S4). The nitrobenzene molecules in position 2 change their relative orientation during the conversion from HS to LS, reducing the number of short contacts and impacting directly on the strength of this interaction. This internal pressure effect is then softened and the direct conversion to LS is then favored.

The interactions between the guests and the MOF are also reflected in the projected density of states (PDOS), as shown in Fig. 7, S1 and S2. The PDOS show the participation of Fe, pyridyl groups and guest molecules on the occupied and empty states of the whole system, i.e., the mixing of the orbitals of the guest molecules and the host crystal bands. The states of the guest molecules are stabilized by both the adsorption on the MOF and the contacts with neighbor molecules. They present a remarkable mixing with the pyridyl groups, that reflect the interaction provided by the π-π and σ-π contacts. The degree of hybridization (mixing) is different for nitrobenzene and naphthalene as expected, the nitrobenzene states being in general at lower energy than the naphthalene ones. Hence, the highest occupied band centred on the pyridyl ligands is highly mixed with the HOMO-1 of naphthalene (region II), but it is not hybridized with the nitrobenzene molecules. Nitrobenzene molecules are instead highly mixed with the HOMO-1 states of pyridyl, corresponding to region I in Fig. 7. In the case of **1-naph**, in this region only naphthalene molecules in position 2 presents a certain mixing with pyridyl bands.

Finally, the analysis of the vibration modes of the system provides additional insight about the ways the guest molecules modulate the host properties and could significantly contribute to the spin transition in one or two steps [9,76]. The large number of vibration modes prevents an exhaustive analysis, but some clues can be obtained from the comparison of a selected set of them. Hence, Fig. 8 shows the C≡N stretching modes of the Pt-cyanide units for **1-naph** and **1-nitro** in the different spin states (Fig. S6 and animated gif files as supporting material). Notice that these N atoms occupy the equatorial positions in the Fe coordination spheres, then they are directly involved in the structural changes accompanying the spin transition. These modes present higher frequencies for **1-naph** than **1-nitro** in both spin states. These C≡N

Table 3
Host-guest and guest-guest interaction energy (kJ/mol) for **1-naph** and **1-nitro**.

Interaction	1-naph		1-nitro	
	HSHS	LSLS	HSHS	LSLS
host-guest	−107.7	−109.2	−101.5	−103.5
host-G1	−94.4	−95.8	−95.1	−99.4
host-G2	−89.6	−92.6	−82.9	−84.1
intermolecular G1-G2	−37.9	−37.8	−29.7	−30.3
intermolecular G2-G2	−26.7	−26.6	−23.6	−11.3

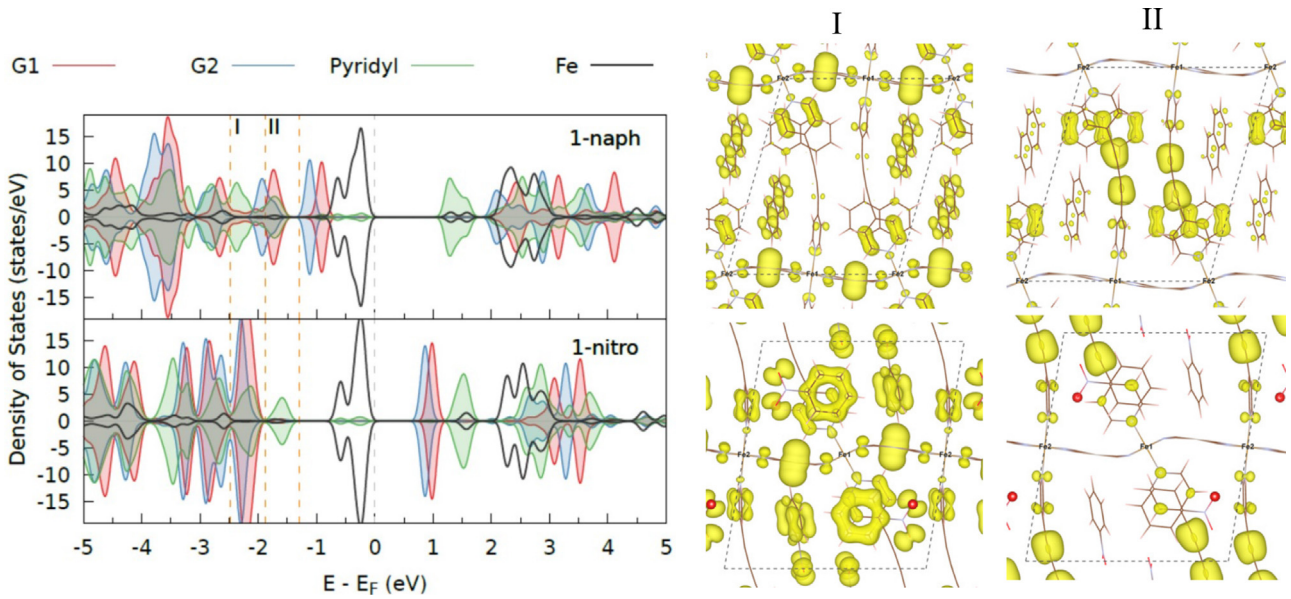

Fig. 7. (Left) Projected density of states of **1-naph** and **1-nitro** on Fe, guest molecules on position 1 and 2 (G1 and G2) and pyridyl groups for LSLS state. (right) Partial electronic density for regions I and II corresponding to the energy windows [E_F-2.48, E_F-1.88] eV and [E_F-1.88, E_F-1.30] eV, respectively (isosurface value = 0.01 e/bohr^3).

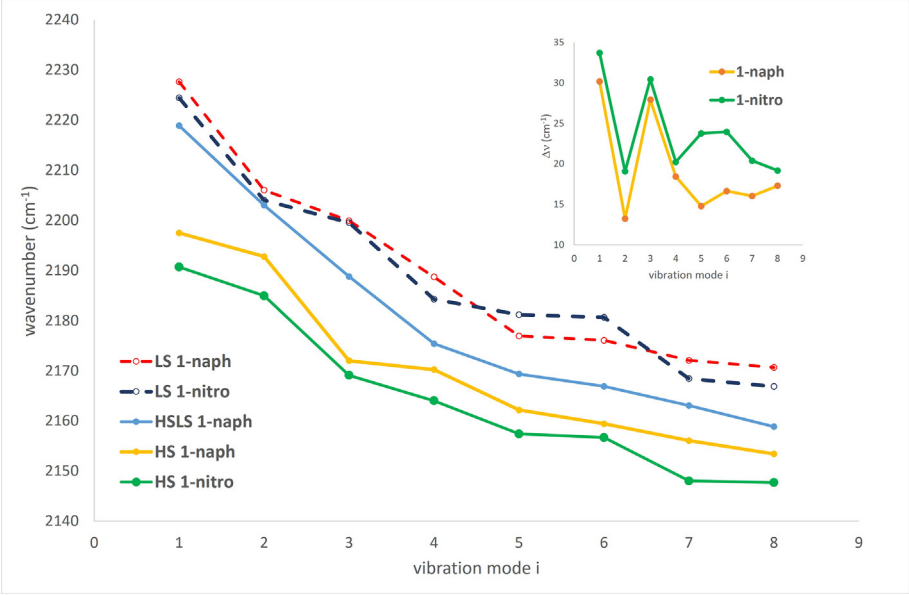

Fig. 8. Evolution of the C≡N stretching modes for **1-nitro** and **1-naph** in the different spin states. The inset shows the frequency change when moving from HS to LS form.

stretching modes red-shift in the transition from LS to HS, the C—N bonds are weakened, and this helps the volumetric expansion from LS to HS. Similar trends are observed in some vibrational modes of the metal-organic framework Fe(1,2,3-triazolate)$_2$ [77]. The red-shift is larger for **1-nitro** than **1-naph** as shown in the inset of Fig. 8. In other words, these modes impart larger amount of vibrational energy to the lattice in the case of **1-nitro**, easing a single step transition. Interestingly the frequencies of the intermediate state of **1-naph** are in average closer to those of the LSLS state than the HSHS state, in line with the stabilization observed for this mixed state with respect to the barycenter of the HSHS-LSLS gap.

Supplementary video related to this article can be found at https://doi.org/10.1016/j.mtchem.2023.101489

Additionally, in the case of **1-nitro** some of the vibration modes of the host are coupled to those of the guest, such as the C=N tension of pyridine rings (these N atoms occupy the axial positions in the Fe octahedrons) with the asymmetric stretching of NO_2 groups (1506 cm^{-1}) and breathing of the nitrobenzene ring (1005 cm^{-1}). Even more, vibrational modes such as the rocking of the pyridyl rings at 845 cm^{-1} (843 cm^{-1} in system **1-nitro**) are less intense in system **1-naph** due to the π-π stacking of naphthalene with the pyridyl groups, weakening the amplitude of the vibration.

Considered together, all these complementary elements suggest the existence of elastic frustrations [78] in the case of **1-naph,** correlated with the stronger host-guest and guest-guest interactions, that prevent the direct conversion from HS to LS, and favors instead the presence of the intermediate state.

4. Conclusions

Several effects have been invoked to explain the guest-dependent spin-transition behavior of Fe^{II} Hofmann-type coordination polymers, and different routes have been explored to control the way the guest modulates the spin-crossover (SCO) properties. The subtle interplay between electronic, structural and steric effects makes it difficult to establish a universal relationship that allows to interpret and predict the magnetic properties of these systems. In this work we have explored the possibility of isolating and quantifying the dominant effects governing the occurrence of one-step or two-step spin transitions in $[Fe(bpb)Pt(CN)_4]$ Hofmann clathrates by means of a computational strategy combining DFT periodic calculations of the whole system, CASSCF/NEVPT2 calculations on monometallic fragments and the plots of the reduced density gradients obtained with the promolecular version of NCI approach. Three main aspects have been analyzed: the ligand field on metallic sites, the stability of the mixed state and the intermolecular interactions.

Our results indicate that the ligand field of each Fe site is almost independent of the guest molecule. Nitrobenzene and naphthalene modify in a similar way the Fe ligand field, despite their different size (107.1 and 121.8 A^3, respectively) [23], different polarity (non-negligible dipole moment for nitrobenzene, while naphthalene is non-polar) and the presence of the electron withdrawing NO_2 group in nitrobenzene, that could indirectly alter the electron density distribution around the Fe center. This result is in line with the structural similarities of Fe sites in both compounds, collected in Table 1.

On the other hand, the stabilization of the mixed state with respect to the halfway point of the total enthalpy change between the HS and the LS states is considered a necessary condition for the occurrence of a two-step transition. The computed relative energy for the intermediate states reveals that this condition is fulfilled in the case of **1-naph**, but not in **1-nitro**, in agreement with the single-step transition observed for the latter. Together with the intramolecular interactions, a significant cooperativity inside the crystal lattice is required to exhibit a two-step transition [66]. In our case, this cooperativity is reflected in the nature and strength of the host-guest and guest-guest intermolecular interactions, that can be separately evaluated. Both systems present the same kind of non-covalent interactions, but they are stronger for naphthalene than nitrobenzene, and slightly spin-dependent, higher for LS than HS state, a fact that can be related to the increasing number of short contacts accompanying the volume reduction when going from HS to LS state. Our calculations allow to distinguish between the two crystallographic different positions occupied by the guest, which adsorption energies reveal the nature of the interactions with the host. Unexpectedly, the intermolecular guest-guest interactions are particularly strong, in special for naphthalene, representing an additional contribution in favor of a two-step transition. Both the presence and strength of these interactions are evidenced by the analysis based on the reduced density gradients, represented by green gradient isosurfaces in Fig. 6, and manifested also in the projected density of states. Finally, our calculations also show the role of the vibronic effects on the guest-dependent SCO transition, how the nature of the guest modulates in different way the vibrational energy of the host, introducing elastic frustration that can prevent the direct conversion from HS to LS state.

Credit author statement

David Arias-Olivares: Investigation, Visualization, Writing-Original draft preparation. **Rocío Sánchez-de-Armas:** Supervision, Conceptualization, Funding acquisition. **Carmen J. Calzado:** Supervision, Conceptualization, Funding acquisition, Methodology, Writing-Reviewing and Editing.

Declaration of competing interest

The authors declare that they have no known competing financial interests or personal relationships that could have appeared to influence the work reported in this paper.

Data availability

Data will be made available on request.

Acknowledgments

The authors acknowledge to Consejería de Economía, Conocimiento, Empresas y Universidad (Junta de Andalucía) and European Regional Development Fund (ERDF) under "Programa Operativo FEDER 2014–2020", project US1380922 for financial support. The technical support of the Supercomputing Team of the Centro Informático Científico de Andalucía (CICA) and the access to the computational facilities of the "Centro de Servicios de Informática y Redes de Comunicaciones" (CSIRC, Universidad de Granada, Spain) are also acknowledged.

Appendix A. Supplementary data

Supplementary data to this article can be found online at https://doi.org/10.1016/j.mtchem.2023.101489.

References

[1] T. Kitazawa, Y. Gomi, M. Takahashi, M. Takeda, M. Enomoto, A. Miyazaki, T. Enoki, Spin-crossover behaviour of the coordination polymer FeII(C5H5N)2NiII(CN)4, J. Mater. Chem. 6 (1996) 119–121.
[2] L.A. Piñeiro-López, F.J. Valverde-Muñoz, M. Seredyuk, M.C. Muñoz, M. Haukka, J.A. Real, Guest induced strong cooperative one- and two-step spin transitions in highly porous iron(II) hofmann-type metal–organic frameworks, Inorg. Chem. 56 (2017) 7038–7047.
[3] J.E. Clements, J.R. Price, S.M. Neville, C.J. Kepert, Hysteretic four-step spin crossover within a three-dimensional porous hofmann-like material, Angew. Chem. Int. Ed. 55 (2016) 15105–15109.
[4] R. Ohtani, S. Hayami, Guest-dependent spin-transition behavior of porous coordination polymers, Chem. Eur J. 23 (2017) 2236–2248.
[5] M.C. Muñoz, J.A. Real, Thermo-, piezo-, photo- and chemo-switchable spin crossover iron(II)-metallocyanate based coordination polymers, Coord. Chem. Rev. 255 (2011) 2068–2093.
[6] C. Bartual-Murgui, A. Akou, C. Thibault, G. Molnár, C. Vieu, L. Salmon, A. Bousseksou, Spin-crossover metal–organic frameworks: promising materials for designing gas sensors, J. Mater. Chem. C 3 (2015) 1277–1285.
[7] V. Rubio-Giménez, S. Tatay, C. Martí-Gastaldo, Electrical conductivity and magnetic bistability in metal–organic frameworks and coordination polymers: charge transport and spin crossover at the nanoscale, Chem. Soc. Rev. 49 (2020) 5601–5638.
[8] A. Bousseksou, G. Molnár, L. Salmon, W. Nicolazzi, Molecular spin crossover phenomenon: recent achievements and prospects, Chem. Soc. Rev. 40 (2011) 3313–3335.
[9] G. Molnár, M. Mikolasek, K. Ridier, A. Fahs, W. Nicolazzi, A. Bousseksou, Molecular spin crossover materials: review of the lattice dynamical properties, Ann. Phys. 531 (2019), 1900076.
[10] K.S. Kumar, M. Ruben, Sublimable spin crossover complexes: from spin-state switching to molecular devices, Angew. Chem. Int. Ed. 60 (2021) 7502–7521.
[11] K. Senthil Kumar, M. Ruben, Emerging trends in spin crossover (SCO) based functional materials and devices, Coord. Chem. Rev. 346 (2017) 176–205.
[12] P. Gütlich, A. Hauser, H. Spiering, Thermal and optical switching of iron(II) complexes, Angew. Chem. Int. Ed. 33 (1994) 2024–2054.
[13] M. Gruber, V. Davesne, M. Bowen, S. Boukari, E. Beaurepaire, W. Wulfhekel, T. Miyamachi, Spin state of spin-crossover complexes: from single molecules to ultrathin films, Phys. Rev. B 89 (2014), 195415.
[14] L. Zhao, Y.-S. Meng, Q. Liu, O. Sato, Q. Shi, H. Oshio, T. Liu, Switching the magnetic hysteresis of an [Fe^{II}–NC–W^{V}]-based coordination polymer by photoinduced reversible spin crossover, Nat. Chem. 13 (2021) 698–704.
[15] B.J.P. Connolly, V. Brosius, N. Mertes, C. Demidova, J.K. Bilyj, M.J. Riley, P.V. Bernhardt, Temperature and counterion dependent spin crossover in a hexaamineiron(II) complex, Eur. J. Inorg. Chem. 2021 (2021) 3938–3949.

[16] T. Liang, F. Zhang, X. Zhang, X. Chen, S. Chen, H. Lou, Z. Zeng, D. Xu, K. Yang, Y. Xiao, P. Chow, B. Shen, Q. Zeng, Pressure-induced spin crossover in a Fe78Si9B13 metallic glass, J. Appl. Phys. 129 (2021), 165901.
[17] J.-F. Dayen, N. Konstantinov, M. Palluel, N. Daro, B. Kundys, M. Soliman, G. Chastanet, B. Doudin, Room temperature optoelectronic devices operating with spin crossover nanoparticles, Mater. Horiz. 8 (2021) 2310–2315.
[18] K.S. Murray, The development of spin-crossover research, Spin?Crossover Mater (2013) 1–54.
[19] M. Seredyuk, K. Znovjyak, F.J. Valverde-Muñoz, I. da Silva, M.C. Muñoz, Y.S. Moroz, J.A. Real, 105 K wide room temperature spin transition memory due to a supramolecular latch mechanism, J. Am. Chem. Soc. 144 (2022) 14297–14309.
[20] S. Schönfeld, W. Bauer, S. Thallmair, G. Hörner, B. Weber, Running in the family: molecular factors controlling spin crossover of iron(II) complexes with schiff-base like ligands, Z. Anorg. Allg. Chem. 647 (2021) 905–914.
[21] M. Carmen Muñoz, J. Antonio Real, Polymeric spin-crossover materials, Spin? Crossover Mater (2013) 121–146.
[22] X. Bao, H.J. Shepherd, L. Salmon, G. Molnár, M.-L. Tong, A. Bousseksou, The effect of an active guest on the spin crossover phenomenon, Angew. Chem. Int. Ed. 52 (2013) 1198–1202.
[23] Z.-P. Ni, J.-L. Liu, M.N. Hoque, W. Liu, J.-Y. Li, Y.-C. Chen, M.-L. Tong, Recent advances in guest effects on spin-crossover behavior in Hofmann-type metal-organic frameworks, Coord. Chem. Rev. 335 (2017) 28–43.
[24] D. Aravena, Z.A. Castillo, M.C. Muñoz, A.B. Gaspar, K. Yoneda, R. Ohtani, A. Mishima, S. Kitagawa, M. Ohba, J.A. Real, E. Ruiz, Guest modulation of spin-crossover transition temperature in a porous iron(II) metal–organic framework: experimental and periodic DFT studies, Chem. Eur J. 20 (2014) 12864–12873.
[25] B. Brachňaková, J. Moncoľ, J. Pavlik, I. Šalitroš, S. Bonhommeau, F.J. Valverde-Muñoz, L. Salmon, G. Molnár, L. Routaboul, A. Bousseksou, Spin crossover metal–organic frameworks with inserted photoactive guests: on the quest to control the spin state by photoisomerization, Dalton Trans. 50 (2021) 8877–8888.
[26] Y. Li, M. Liu, Z.-S. Yao, J. Tao, Temperature-dependent hysteretic two-step spin crossover in two-dimensional Hofmann-type compounds, Dalton Trans. 49 (2020) 7245–7251.
[27] I.S. Kuzevanova, O.I. Kucheriv, V.M. Hiiuk, D.D. Naumova, S. Shova, S.I. Shylin, V.O. Kotsyubynsky, A. Rotaru, I.O. Fritsky, I.Y.A. Gural'skiy, Spin crossover in iron(ii) Hofmann clathrates analogues with 1,2,3-triazole, Dalton Trans. 50 (2021) 9250–9258.
[28] L. Piñeiro-López, M. Seredyuk, M.C. Muñoz, J.A. Real, Effect of guest molecules on spin transition temperature in loaded hofmann-like clathrates with improved porosity, Eur. J. Inorg. Chem. 2020 (2020) 764–769.
[29] K. Hosoya, S.-I. Nishikiori, M. Takahashi, T. Kitazawa, Spin-crossover behavior of hofmann-type-like complex Fe(4,4'-bipyridine)Ni(CN)$_4$·nH2O depending on guest species, Magnetochemistry 2 (2016) 8.
[30] F.J. Valverde-Muñoz, C. Bartual-Murgui, L. Piñeiro-López, M.C. Muñoz, J.A. Real, Influence of host–guest and host–host interactions on the spin-crossover 3D hofmann-type clathrates {Fe^{II}(pina)[M^{I}(CN)$_2$]$_2$}·xMeOH (M^{I} = Ag, Au), Inorg. Chem. 58 (2019) 10038–10046.
[31] C.-J. Zhang, K.-T. Lian, G.-Z. Huang, S. Bala, Z.-P. Ni, M.-L. Tong, Hysteretic four-step spin-crossover in a 3D Hofmann-type metal–organic framework with aromatic guest, Chem. Commun. (J. Chem. Soc. Sect. D) 55 (2019) 11033–11036.
[32] Á. Fernández-Blanco, L.A. Mariano, L. Piñeiro-López, J.A. Real, J.S. Costa, R. Poloni, J.A. Rodríguez-Velamazán, Hidden ordered structure in the archetypical Fe(pyrazine)[Pt(CN)4] spin-crossover porous coordination compound, CrystEngComm 24 (2022) 6349–6356.
[33] V.M. Hiiuk, S.I. Shylin, D.D. Barakhtii, D.M. Korytko, V.O. Kotsyubynsky, A. Rotaru, S. Shova, I.y.A. Gural'skiy, Two-step spin crossover in hofmann-type coordination polymers [Fe(2-phenylpyrazine)$_2${M(CN)$_2$}$_2$] (M = Ag, Au), Inorg. Chem. 61 (2022) 2093–2104.
[34] F.-L. Liu, D. Li, L.-J. Su, J. Tao, Reversible three equal-step spin crossover in an iron(ii) Hofmann-type metal–organic framework, Dalton Trans. 47 (2018) 1407–1411.
[35] L. Piñeiro-López, M. Seredyuk, M.C. Muñoz, J.A. Real, Two- and one-step cooperative spin transitions in Hofmann-like clathrates with enhanced loading capacity, Chem. Commun. (J. Chem. Soc. Sect. D) 50 (2014) 1833–1835.
[36] G. Kresse, J. Hafner, Ab initio molecular-dynamics for liquid-metals, Phys. Rev. B 47 (1993) 558–561.
[37] G. Kresse, J. Hafner, Ab-initio molecular-dynamics simulation of the liquid.-metal amorphous-semiconductor transition in Germanium, Phys. Rev. B 49 (1994) 14251–14269.
[38] G. Kresse, J. Furthmuller, Efficient iterative schemes for ab initio total-energy calculations using a plane-wave basis set, Phys. Rev. B 54 (1996) 11169–11186.
[39] G. Kresse, J. Furthmuller, Efficiency of ab-initio total energy calculations for metals and semiconductors using a plane-wave basis set, Comput.l Mater. Sci. 6 (1996) 15–50.
[40] B. Hammer, L.B. Hansen, J.K. Nørskov, Improved adsorption energetics within density-functional theory using revised Perdew-Burke-Ernzerhof functionals, Phys. Rev. B 59 (1999) 7413–7421.
[41] N. Montenegro-Pohlhammer, R. Sánchez-de-Armas, C.J. Calzado, Deposition of the spin crossover FeII–pyrazolylborate complex on Au(111) surface at the molecular level, Chem. Eur J. 27 (2021) 712–723.
[42] R. Sanchez-de-Armas, N. Montenegro-Pohlhammer, A. Develioglu, E. Burzuri, C.J. Calzado, Spin-crossover complexes in nanoscale devices: main ingredients of the molecule-substrate interactions, Nanoscale 13 (2021) 18702–18713.
[43] J. Villalva, A. Develioglu, N. Montenegro-Pohlhammer, R. Sánchez-de-Armas, A. Gamonal, E. Rial, M. García-Hernández, L. Ruiz-Gonzalez, J.S. Costa, C.J. Calzado, E.M. Pérez, E. Burzurí, Spin-state-dependent electrical conductivity in single-walled carbon nanotubes encapsulating spin-crossover molecules, Nat. Commun. 12 (2021) 1578.
[44] N. Montenegro-Pohlhammer, R. Sánchez-de-Armas, C.J. Calzado, M. Borges-Martínez, G. Cárdenas-Jirón, A photo-induced spin crossover based molecular switch and spin filter operating at room temperature, Dalton Trans. 50 (2021) 6578–6587.
[45] S. Grimme, J. Antony, S. Ehrlich, H. Krieg, A consistent and accurate ab initio parametrization of density functional dispersion correction (DFT-D) for the 94 elements H-Pu, J. Chem. Phys. 132 (2010), 154104.
[46] S. Grimme, S. Ehrlich, L. Goerigk, Effect of the damping function in dispersion corrected density functional theory, J. Comput. Chem. 32 (2011) 1456–1465.
[47] G. Kresse, D. Joubert, From ultrasoft pseudopotentials to the projector augmented-wave method, Phys. Rev. B 59 (1999) 1758–1775.
[48] G. Molnar, S. Rat, L. Salmon, W. Nicolazzi, A. Bousseksou, Spin crossover nanomaterials: from fundamental concepts to devices, Adv. Mater. 30 (2018).
[49] S. Vela, M. Fumanal, J. Ribas-Arino, V. Robert, Towards an accurate and computationally-efficient modelling of Fe(II)-based spin crossover materials, Phys. Chem. Chem. Phys. 17 (2015) 16306–16314.
[50] D.G.M. Atanasov, K. Sivalingam, F. Neese, A modern first-principles view on ligand field theory through the eyes of correlated multireference wavefunctions, Struct. Bond 143 (2012) 149–220.
[51] F. Neese, The ORCA program system, WIREs Comput. Mol. Sci. 2 (2012) 73–78.
[52] C. Angeli, R. Cimiraglia, S. Evangelisti, T. Leininger, J.-P. Malrieu, Introduction of n-electron valence states for multireference perturbation theory, J. Chem. Phys. 114 (2001) 10252–10264.
[53] C. Angeli, R. Cimiraglia, J.-P. Malrieu, n-electron valence state perturbation theory: a spinless formulation and an efficient implementation of the strongly contracted and of the partially contracted variants, J. Chem. Phys. 117 (2002) 9138–9153.
[54] C. Angeli, R. Cimiraglia, J.-P. Malrieu, N-electron valence state perturbation theory: a fast implementation of the strongly contracted variant, Chem. Phys. Lett. 350 (2001) 297–305.
[55] C. Angeli, S. Borini, M. Cestari, R. Cimiraglia, A quasidegenerate formulation of the second order n-electron valence state perturbation theory approach, J. Chem. Phys. 121 (2004) 4043–4049.
[56] A. Schäfer, H. Horn, R. Ahlrichs, Fully optimized contracted Gaussian basis sets for atoms Li to Kr, J. Chem. Phys. 97 (1992) 2571–2577.
[57] F. Weigend, Accurate Coulomb-fitting basis sets for H to Rn, Phys. Chem. Chem. Phys. 8 (2006) 1057–1065.
[58] F. Weigend, R. Ahlrichs, Balanced basis sets of split valence, triple zeta valence and quadruple zeta valence quality for H to Rn: design and assessment of accuracy, Phys. Chem. Chem. Phys. 7 (2005) 3297–3305.
[59] R.A. Boto, F. Peccati, R. Laplaza, C. Quan, A. Carbone, J.-P. Piquemal, Y. Maday, J. Contreras-García, NCIPLOT4: fast, robust, and quantitative analysis of non-covalent interactions, J. Chem. Theor. Comput. 16 (2020) 4150–4158.
[60] M. Ernst, G. Gryn'ova, Strength and nature of host-guest interactions in metal-organic frameworks from a quantum-chemical perspective, ChemPhysChem 23 (2022), e202200098.
[61] E.R. Johnson, S. Keinan, P. Mori-Sánchez, J. Contreras-García, A.J. Cohen, W. Yang, Revealing noncovalent interactions, J. Am. Chem. Soc. 132 (2010) 6498–6506.
[62] R. Laplaza, F. Peccati, D. Arias-Olivares, J. Contreras-García, 14 Visualizing non-covalent interactions with NCIPLOT, in: G. Simon (Ed.), Complementary Bonding Analysis, De Gruyter, Berlin, Boston, 2021, pp. 353–378.
[63] J. Contreras-García, R.A. Boto, F. Izquierdo-Ruiz, I. Reva, T. Woller, M. Alonso, A benchmark for the non-covalent interaction (NCI) index or… is it really all in the geometry? Theor. Chem. Acc. 135 (2016) 242.
[64] E.K. Wieduwilt, G. Macetti, R. Scatena, P. Macchi, A. Genoni, Extending libraries of extremely localized molecular orbitals to metal organic frameworks: a preliminary investigation, Crystals 11 (2021) 207.
[65] W. Humphrey, A. Dalke, K. Schulten, VMD: visual molecular dynamics, J. Mol. Graph. 14 (1996) 33–38.
[66] J.A. Real, H. Bolvin, A. Bousseksou, A. Dworkin, O. Kahn, F. Varret, J. Zarembowitch, Two-step spin crossover in the new dinuclear compound [Fe(bt)(NCS)2]2bpym, with bt = 2,2'-bi-2-thiazoline and bpym = 2,2'-bipyrimidine: experimental investigation and theoretical approach, J. Am. Chem. Soc. 114 (1992) 4650–4658.
[67] V. Ksenofontov, A.B. Gaspar, V. Niel, S. Reiman, J.A. Real, P. Gütlich, On the nature of the plateau in two-step dinuclear spin-crossover complexes, Chem. Eur J. 10 (2004) 1291–1298.
[68] S. Zein, S.A. Borshch, Energetics of binuclear spin transition complexes, J. Am. Chem. Soc. 127 (2005) 16197–16201.
[69] J. Cirera, E. Ruiz, Theoretical modeling of two-step spin-crossover transitions in FeII dinuclear systems, J. Mater. Chem. C 3 (2015) 7954–7961.
[70] K.P. Kepp, Theoretical study of spin crossover in 30 iron complexes, Inorg. Chem. 55 (2016) 2717–2727.
[71] O.S. Siig, K.P. Kepp, Iron(II) and iron(III) spin crossover: toward an optimal density functional, J. Phys. Chem. A 122 (2018) 4208–4217.
[72] J. Cirera, E. Ruiz, Computational modeling of transition temperatures in spin-crossover systems, Comments Mod. Chem. 39 (2019) 216–241.

[73] J. Cirera, M. Via-Nadal, E. Ruiz, Benchmarking density functional methods for calculation of state energies of first row spin-crossover molecules, Inorg. Chem. 57 (2018) 14097−14105.
[74] M. Ohlrich, B.J. Powell, Fast, accurate enthalpy differences in spin crossover crystals from DFT+U, J. Chem. Phys. 153 (2020), 104107.
[75] P.D. Southon, L. Liu, E.A. Fellows, D.J. Price, G.J. Halder, K.W. Chapman, B. Moubaraki, K.S. Murray, J.F. Létard, C.J. Kepert, Dynamic interplay between spin-crossover and host-guest function in a nanoporous metal-organic framework material, J. Am. Chem. Soc. 131 (2009) 10998−11009.
[76] J.A. Wolny, R. Diller, V. Schünemann, Vibrational spectroscopy of mono- and polynuclear spin-crossover systems, Eur. J. Inorg. Chem. 2012 (2012) 2635−2648.
[77] A.B. Andreeva, K.N. Le, K. Kadota, S. Horike, C.H. Hendon, C.K. Brozek, Cooperativity and metal−linker dynamics in spin crossover framework Fe(1,2,3-triazolate)2, Chem. Mater. 33 (2021) 8534−8545.
[78] M. Paez-Espejo, M. Sy, K. Boukheddaden, Elastic frustration causing two-step and multistep transitions in spin-crossover solids: emergence of complex antiferroelastic structures, J. Am. Chem. Soc. 138 (2016) 3202−3210.